MOTION COMPENSATION FOR SQUINT MODE SPOTLIGHT SAR IMAGING USING EFFICIENT 2D INTERPOLATION

K.-T. Kim[1], J.-I. Park[1], and S.-H. Park[2, *]

[1]Department of Electronic Engineering, Pohang University of Science and Technology, Pohang, Korea

[2]Department of Electronic Engineering, Pukyong National University, Busan, Korea

Abstract—In the squint mode airborne spotlight synthetic aperture radar system using the range migration algorithm (RMA), autofocus (AF) technique yields poor results due to the squint spreading of the point spread function (PSF) of a scatterer. Thus, two-dimensional (2D) interpolation is required to direct PSF blurring in cross-range direction, to improve the cross-range resolution Δy and to remove the spatially-varying sidelobe. Because conventional 2D interpolation requires huge computation time and yields large computation errors, we propose an efficient 2D interpolation technique for squint-mode RMA composed of two 1D interpolations. Simulation results using the measured turbulence data show Δy was improved considerably and PSF was successfully focused by the proposed method with a reduced computation time.

1. INTRODUCTION

Synthetic aperture radar (SAR) is an efficient radar imaging technology that provides two dimensional (2D) high resolution radar cross section (RCS) [1–3] of ground targets at a long range and has been used for many applications along with its inverse type ISAR [4–23]. The main idea of this technique is to obtain a long aperture enough to provide high cross-range resolution Δy using a radar carried by a moving airborne vehicle. The widely used method for the fine-resolution image of a localized region is the spotlight mode [4–23]; in

this mode, the radar steers its antenna beam to continuously illuminate the imaged area. Among several SAR algorithms, the range migration algorithm (RMA) [4, 14] is widely used because it is much faster and simpler than other algorithms due to its one-dimensional (1D) spectrum interpolation.

The biggest challenge in spotlight SAR imaging using RMA is the aircraft deviation from the nominal trajectory due to the effect of turbulence. This trajectory error is compensated for using the measured trajectory data. However, the residual sensor error causes the image to be blurred and the image must be focused using an autofocus (AF) technique for each range bin. In the broadside spotlight SAR imaging in which $\theta = 90°$, where θ is the angle between the flight direction and a vector from the trajectory center to the scene center, the cross-range component of the point spread function (PSF) of a scatterer (SC) spreads in one or a small number of down-range bins. Therefore, the autofocus (AF) technique provides a well-focused PSF. However, in the squint mode ($\theta \neq 90°$), the cross-range component spreads in squint direction over several range bins and AF technique cannot focus the image due to the mismatch between the direction of PSF blurring and that of autofocus. Therefore, the SAR data in the squint must be converted to that in the broadside mode.

This paper proposes a motion compensation (MOCOM) method for squint mode RMA spotlight SAR imaging under turbulence. The proposed method converts the squint mode SAR data to that in broadside mode using a fast and efficient 2D interpolation method and the resultant broadside mode SAR image is autofocused successfully. For this purpose, we modeled the aircraft trajectory under turbulence using the measured spectrum data of turbulence. In simulations using an SC, the modeled trajectory under turbulence and the entropy minimization method for autofocus, PSF was successfully focused by the proposed method yielding higher accuracy and more reduced computation time than the existing 2D interpolation method. Furthermore, Δy dependent on the squint angle was significantly improved by the proposed method.

2. BASIC PRINCIPLES AND PROPOSED METHOD

2.1. RMA for Spotlight Mode SAR Imaging

Assuming a SC n with an amplitude σ_n is located at (x_n, y_n) and a radar located at $(0, u)$ transmits a wideband chirp signal $p(t)$ and the radar beam is steered toward the scene center at each $(0, u)$, the

reflected signal collected at $(0, u)$ from N SCs can be expressed by [4]

$$s(t, u) = \sum_{n=1}^{N} \sigma_n p \left[t - \frac{2\sqrt{x_n^2 + (y_n - u)^2}}{c} \right] \quad (1)$$

Here, $2\sqrt{x_n^2 + (y_n - u)^2}/c$ is the two-way time delay between the radar and the SC n and c the speed of the light. In 3D modeling, x_n is x_{sn} which is the slant range of the target, satisfying $x_{sn}^2 = x_n^2 + z_n^2$, where z_n is the location of the SC in z axis. The final goal of SAR imaging algorithm is to position σ_n at (x_n, y_n) using (1).

RMA to derive SAR image using (1) is composed of four steps [4, 14]; 2D Fourier transform (FT) of $s(t, u)$, 2D matched filtering, 1D interpolation in the frequency of down-range, and final 2D inverse FT. Assuming $-L \leq u \leq L$, the 2D FT of $s(t, u)$ can be derived using the method of stationary phase [4, 14] as follows:

$$s(\omega, k_u) = P(\omega) \sum_n \sigma_n \exp\left(-j\sqrt{4k^2 - k_u^2} x_n - jk_u y_n\right), \quad (2)$$

where ω and k_u are the frequencies of t and u, $k = 2\pi/\lambda$ and λ is the wavelength. If we define $k_x = \sqrt{4k^2 - k_u^2}$ and $k_y = k_u$, (2) can be written as

$$S(\omega, k_u) = P(\omega) F_0(k_x, k_y), \quad (3)$$

where

$$F_0(k_x, k_y) = \sum_n \sigma_n \exp(-jk_x x_n - jk_y y_n), \quad (4)$$

Removing $P(\omega)$ and the baseband conversion can be simultaneously achieved by 2D matched-filtering using the reference signal

$$s_0(t, u) = p\left[t - 2\frac{\sqrt{X_c^2 + (Y_c - u)^2}}{c}\right] \quad (5)$$

$$\Leftrightarrow S_0(\omega, k_u) = P(\omega) \exp[-jk_x X_c - jk_u Y_c], \quad (6)$$

where (X_c, Y_c) is the scene center. The resulting baseband signal is

$$F_b(k_x, k_y) = S(\omega, k_u) S_0^*(\omega, k_u). \quad (7)$$

Because the spectral counterpart of (x_n, y_n) is (k_x, k_y) and k_x not uniformly sampled due to $k_x = \sqrt{4k^2 - k_u^2}$, 1D interpolation is required for uniform grids in k_x direction. Then, the SAR image with amplitude $f(x, y)$ at (x, y) can be obtained by the inverse 2D FT of $F_b(k_x, k_y)$. Because of the 1D interpolation, RMA is faster and more accurate than other SAR algorithms and can be used even at squint angles [4, 14].

2.2. Motion Compensation due to Turbulence and Problem in Squint Mode

Because the aircraft-carrying vehicle may deviate from its planned path due to the aircraft motion in turbulence, motion compensation (MOCOM) is required using the trajectory data measured by the global positioning system (GPS) and inertia measurement unit (IMU). Two types of errors occur in general; along-track and cross-track errors.

The along-track error is caused by the non-uniform emission of radar signals. To remove this type of error, the pulse repetition frequency (PRF) is dynamically controlled to emit radar signals uniformly in space. We assume that an aircraft moves in u-direction from u_0 with a constant velocity v_0 and define t as the fast-time and t_u as the slow-time for convenience. u at t_u is related by the following integration:

$$u(t_u) = u_0 + \int_0^{t_u} v_u(t_u)dt_u, \tag{8}$$

where $v_u(t_u)$ is the aircraft velocity in x-direction at t_u. The optimum pulse emission time t_{Op} for the pth pulse is determined by the following iterative equation:

$$t_{Op}^{(0)} = k\tau_{PRI}, \quad t_{Op}^{(i+1)} = t_{Op}^{(i)} - A/v_u\left(t_{Op}^{(i)} - \tau_L\right), \tag{9}$$

where i is the iteration number, and A is

$$A = u(t_{Op}^{(i)} - \tau_L) + \tau_L v_u\left(t_{Op}^{(i)} - \tau_L\right) - u_0 - v_0 k\tau_{PRI}. \tag{10}$$

τ_L is the sensor reaction time and τ_{PRI} is the pulse repetition interval (see [24] for detailed procedure).

The cross-track error is the error normal to the along-track. For an aircraft moving in y-direction, the cross-track error includes the error in x- and z-directions. When the cross-track error $\Delta r(t_u)$ occurs at each slow-time t_u, the signal in (1) is further delayed by $\Delta r(t_u)$ and in the spectrum of the fast-time, it is represented by the phase addition. This type of error must be removed using the GPS/INS measurement because this will break the coherency between received signals and as a result, SAR image can be seriously blurred. The MOCOM method used in this letter for the cross-track error is a simple phase subtraction corresponding to the deviation $\Delta r(t_u)$ at each slow-time t_u. Using measured trajectory-to-center distance $r(t_u)$ and the nominal trajectory-to-center distance $R(t_u)$, MOCOM is conducted before 2D matched-filtering as follows:

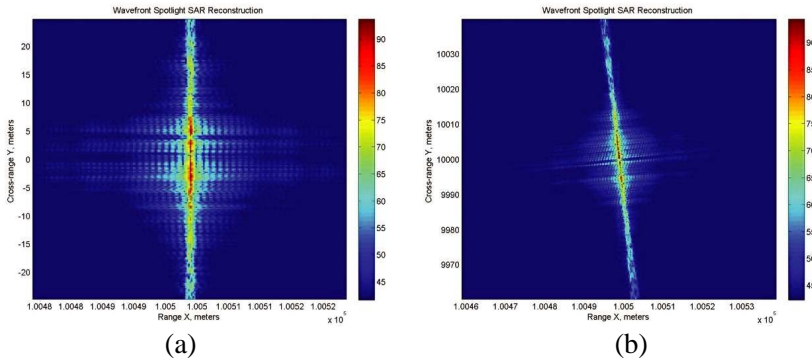$$s_M(\omega, t_u) = s(\omega, t_u)\exp(-jk\Delta r(t_u)). \tag{11}$$

Figure 1. PSF spreading of SAR image due to the sensor error. (a) Broadside. (b) Squint.

Because the measured sensor error causes the PSF of a scatter to be blurred seriously depending on the squint angle, AF technique is required after 1D interpolation to derive the focused image. For this purpose, each cross-range bin of $F_b(x, k_y)$ is multiplied by a phase error that yields the most focused image $f(x, y)$. In this paper, we applied the method of the 2D entropy minimization [25] which utilizes 2D entropy as the image focus.

Because AF is conducted in cross-range direction, the direction of PSF spreading must be identical to the cross-range direction. If it spreads vertically over several range bins, the image can be blurred. Because PSF spreading in broadside mode satisfies this requirement (Figure 1(a)), it can be easily focused by the AF technique. However, in the squint mode, the image cannot be successfully focused due to the PSF blurring in several range bins (Figure 1(b)). Therefore, the SAR data in squint mode should be converted to that in the broadside mode.

Some methods were introduced to convert the squint mode SAR data to improve the image quality [26, 27]. The method in [26] assumes that the squint mode SAR data was not reliable and converted the squint mode SAR data to that in broadside mode using a complicated mathematical procedure. The method proposed in [27] converted the monostatic squint mode SAR data to that in bistatic squint mode to improve the image quality. However, the results in the two papers can be derived once we change interpolation grids in the frequency domain as proposed in this paper.

2.3. Conversion to Broadside Mode Using Proposed 2D Interpolation Method

In the squint mode frequency domain (k_x, k_y) with the squint angle $\theta_c\,(\theta_c = \tan^{-1}(Y_c/X_c))$, the spectrum is rotated by θ_c compared with the broadside mode spectrum (k_{xR}, k_{yR}) as follows (see Figure 2 and [4]):

$$\begin{bmatrix} k_{xR} \\ k_{yR} \end{bmatrix} = \begin{bmatrix} \cos\theta_c & \sin\theta_c \\ -\sin\theta_c & \cos\theta_c \end{bmatrix} \begin{bmatrix} k_x \\ k_y \end{bmatrix} \tag{12}$$

In (k_{xR}, k_{yR}) domain, the PSF in Figure 1(b) can be converted to that in Figure 1(a) if 2D FT is conducted using the uniformly sample spectrum in (k_{xR}, k_{yR}) (Figure 2). However, because the spectrum is non-uniform in (k_{xR}, k_{yR}) domain, 2D interpolation is required to derive uniformly sampled spectrum in (k_{xR}, k_{yR}) domain.

Another benefit of the broadside mode conversion using 2D interpolation is the enhancement of Δy. Contrary to the down-range resolution Δx of RMA algorithm determined by the system operating frequency $(\Delta x \approx \pi c/2\omega_0), \Delta y$ of a SC located at the scene center (x_n, y_n) is spatially varying due to the dependency on the squint angle $\theta c = \tan^{-1}(y_n/x_n)$ and the aperture length L as follows [4]:

$$\Delta y \approx \frac{r_n \lambda_c}{4L \cos\theta_c}, \tag{13}$$

where λ_c is the wavelength at the center frequency and $r_n^2 = (x_n^2 + y_n^2)$. (see [4] for the derivation procedure). As the squint angle becomes
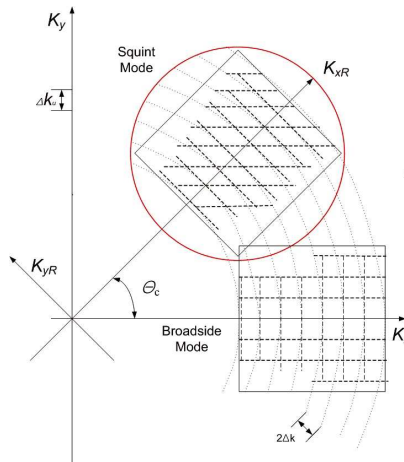

Figure 2. SAR spectrum in broadside and squint modes.

larger, Δy degrades more. This problem can be easily solved by the broadside mode conversion because $\cos \theta_c = 1$ in broadside mode. In addition, in the case of inscribing a rectangular region in the squint mode SAR spectrum to remove the variation of sidelobes of PSFs [4], considerable loss of information in cross-range can occur because of the poor inscription in the rotated spectrum (Figure 2) and as a result, Δy can further degrade. In broadside mode, inscription is easy and doesn't incur considerable loss of information.

Various 2D interpolation methods exist and most of them interpolate the intermediate value by estimating the parameters of 2D interpolation kernel function based on the known values at surrounding points [28]. However, due to $k_x = \sqrt{4k^2 - k_u^2}$ in (2), grids at low frequencies (small k values) are narrowly spaced resulting in small interpolation errors. At high frequencies, grids are widely spaced and the interpolation error is large. The varying interpolation error can degrade the image quality. Furthermore, huge computation is consumed compared with 1D interpolation to estimate the parameters of the kernel function at each point. Therefore, the conventional 2D interpolation methods are not adequate for the real-time SAR signal processing. In this paper, we use the 2D spline interpolation for comparison, which is a widely used method [28].

The 2D interpolation method proposed in this paper is composed of two 1D interpolations; the first interpolation in k_{yR} direction and the second one in k_{xR} direction. Because of the only two 1D interpolations, the proposed method consumes much less time than the conventional 2D interpolation methods. Furthermore, the spatially varying 2D interpolation error can be considerably reduced because of the 1D interpolation error. It is obvious that the 1D interpolation yields considerably less interpolation errors than those by the 2D interpolation. Even though each 1D interpolation may yield interpolation errors, the interpolation error of the two methods is considerably smaller than that of the spatially varying 2D interpolation. This paper reduces the interpolation error by transforming the 2D spatial variation into 1D spatial variation. A similar method was introduced to reduce the computation time for the conventional broadside mode polar format algorithm (PFA) without MOCOM [29]. However, modification is required for RMA under motion due to the difference of the algorithms; RMA is based on the spherical wave while PFA is on the plane wave.

The proposed method utilizes the following relationship among $(k_{xR}, k_{yR}), (k_x, k_y)$ and k:

$$k_x^2 + k_y^2 = k_{xR}^2 + k_{yR}^2 = 4k^2 \qquad (14)$$

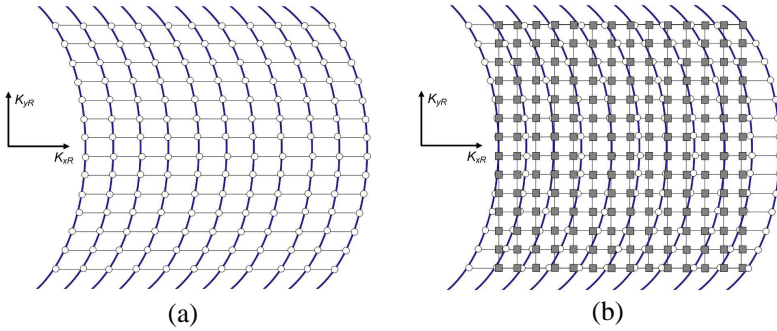The first 1D interpolation is conducted on uniformly spaced k_{yR}

Figure 3. Proposed 2D interpolation composed of two 1D interpolations. (a) First interpolation (k_{yR}). (b) Second interpolation (k_{yR}).

defined as k_{yuni} (circles in Figure 3(a)). Each curve in Figure 3(a) is determined by k in (14) (see Figure 2) and represents the position of SAR spectrum in (k_{xR}, k_{yR}) domain. Because the original SAR spectrum exists in (k_x, k_y), it must be converted to that in (k_{xR}, k_{yR}) using (12). Then, for each k, 1D interpolation is conducted using nonuniform k_{yR} and uniform k_{yuni} yielding the resultant spectrum uniform in k_{yR}. The interpolation error in this is small because only 1D spatial variation is considered.

The second interpolation is conducted in k_{xR} using the spectrum in (k_{xR}, k_{yuni}). Before the interpolation, unknown k_{xR}s corresponding to the interpolated k_{yuni}s must be found using (14). Then, using known uniform points defined as k_{xuni} 1D interpolation is conducted for each k_{yuni} and the resultant points in (k_{xuni}, k_{yuni}) (squares in Figure 3(b)) were uniformly spaced in (k_{xR}, k_{yR}). Compared with the 2D interpolation, the interpolation error is reduced because 2D spatial variation was transformed into 1D spatial variation. The spectrum after the second interpolation is in broadside mode and yields cross-shaped PSF.

3. SIMULATION RESULTS

Three simulations were conducted using the measured power spectral density (PSD) of turbulence and the system parameters in Table 1. For the flight trajectory, Kolmogorov factorization of the PSD [30] was conducted to derive the transfer function of the linear accelerations(x, y and z) and the rotational accelerations (roll, pitch and yaw). Then,

Table 1. System parameters.

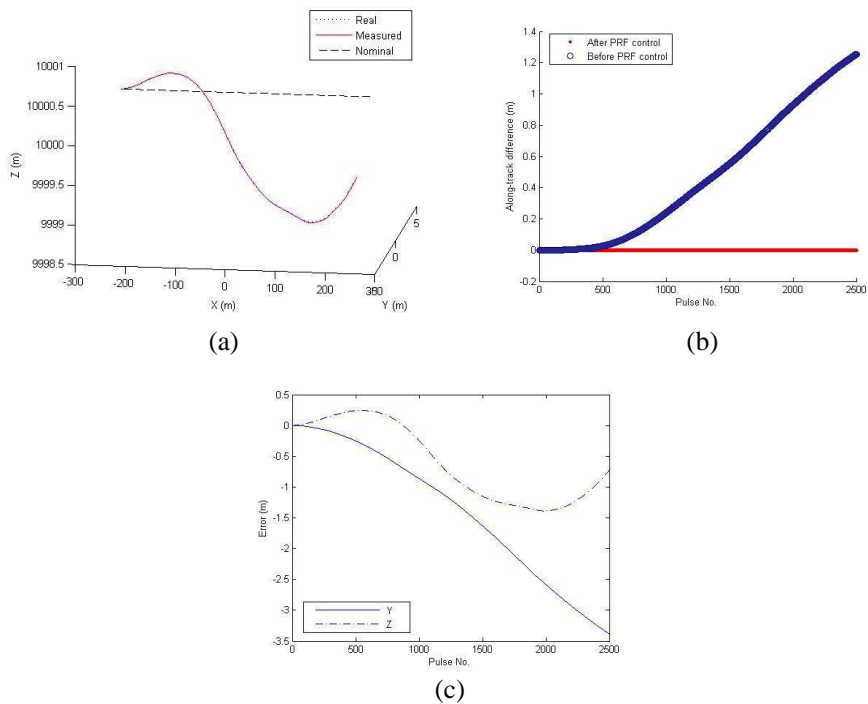| Carrier frequency	9.0 GHz	PRF	500 Hz
Bandwidth	500 MHz	Scene size	$100 \times 100\,\text{m}^2$
Aircraft velocity	[100 0 0] m/s	SCs	Center + [0 0 0] and [50 50 0] m
Sensor reaction time (τ_L)	0.005 s	Pulse Width	2.5 μs
Sampling rate	1.2 GHz	Altitude	10 km

(a)

(b)

(c)

Figure 4. 3D trajectory simulation and along-track difference. (a) 3D trajectory. (b) Along-track (x-direction) difference. (c) Comparison of the error in y- and z-directions.

the acceleration time histories were derived by the convolution of each transfer function and noise and the true aircraft trajectory was calculated by integrating the derived accelerations. The measured trajectory was derived by adding the sensor errors and the PRF control

in (9) was applied to the true and the measured trajectories. The two trajectories were much different from the nominal trajectory due to the turbulence and the along-track (x-direction) error reduced considerably after PRF control (Figure 4(a)). The error in y-direction was larger than the error in z-direction (altitude); the maximum error in y-direction was 3.38 m and that in z-direction was 1.39 m (Figure 4(c)).

In the first simulation, ideal MOCOM using the real position of the aircraft (no sensor error) was conducted to prove the efficiency of the proposed method. The PSFs derived using the 1D spline interpolation [28] were tilted due to the squint angle $\theta_c = 5.71°$ and those using the 2D interpolation were cross-shaped (Figure 5). The SAR image derived using the conventional 2D spline interpolation [28] was contaminated by the two ghost targets (circles in Figure 5(b)) due to spatially varying interpolation errors, however, the ghosts were not seen on the SAR image because the interpolation error
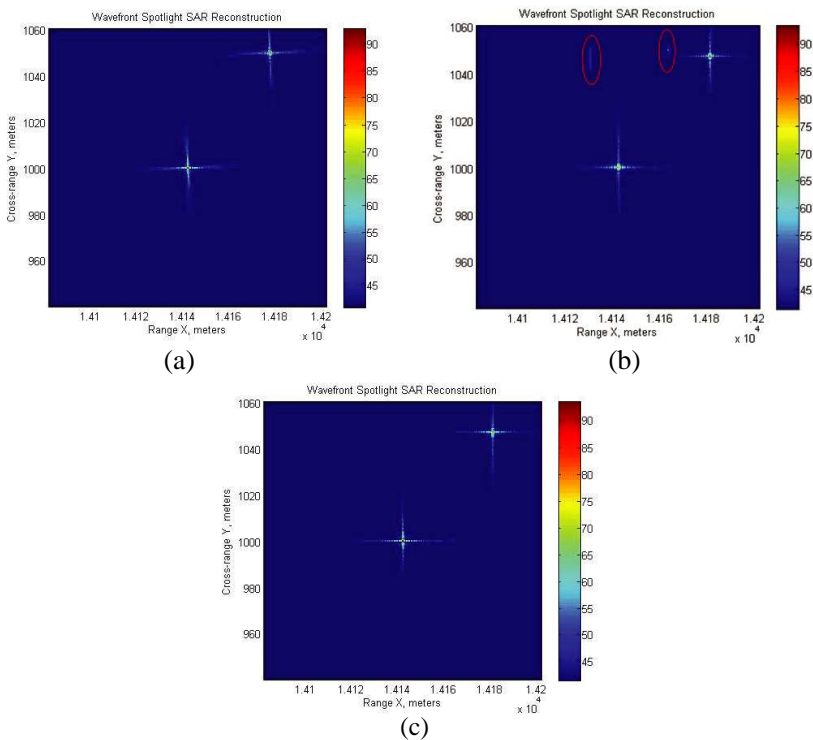

Figure 5. Comparison of SAR images derived from ideal MOCOM. (a) 1D interpolation. (b) 2D interpolation. (c) Proposed method.

Table 2. Comparison of computation time.

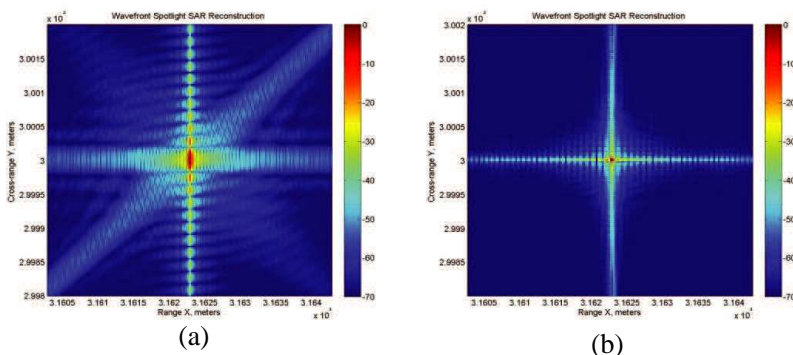|	1D	2D(proposed)	2D (conventional)
Computation time	4.17 s	8.60 s	145.76 s

(a)   (b)

Figure 6. Comparison of SAR images at a high squint angle ($\theta_n(0) = 45°$). (a) 1D interpolation. (b) Proposed method.

considerably reduced due to two 1D interpolations(Figure 5(c)). Due to the two 1D interpolations, the computation time of the proposed method derived using MATLAB and Intel i7 processor is approximately double of that by 1D interpolation and 5.9% of the conventional 2D interpolation (Table 2). This is the result of two 1D spline interpolations which require $O\ (n \log n)$ computations to interpolate one data point using sorted data grids while 2D spline interpolation requires $O\ ((n \log n)^2)$ [31].

The second simulation was conducted to demonstrate the improvement of Δy of the proposed 2D interpolation at a high squint angle. An SC at $[30\ 30\ 0]$ km ($\theta_c = 45°$) was simulated using the same radar parameters and $L = 3$ km. A rectangular region in 2D SAR spectrum was inscribed to compare the SAR image. As mentioned in the subsection 2.3, the SAR image derived using the 1D interpolation is seriously blurred in cross-range direction ($\Delta y = 1.6251$ m) (Figure 6(a)), whereas the image derived using the proposed 2D interpolation is well-focused ($\Delta y = 0.2676$ m) (Figure 6(b)).

In the third simulation, we assumed a long range SAR imaging of an SC and MOCOM was conducted using the measured sensor trajectory. AF using the entropy cost function [25] was applied and the PSF quality was evaluated. The simulation conditions were the same as those in the first simulation except for the $L = 5.732$ km,
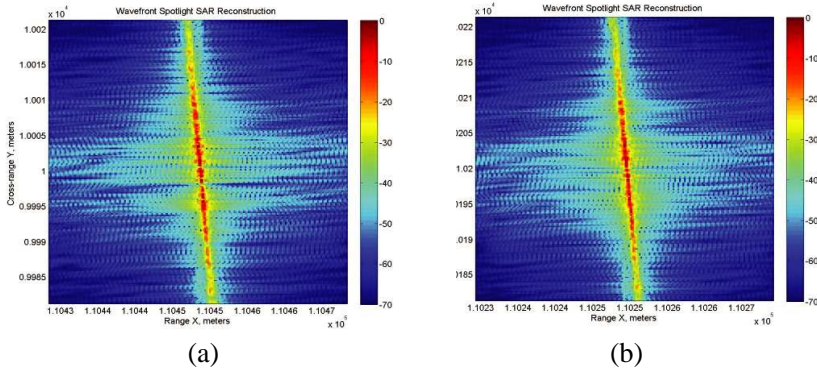
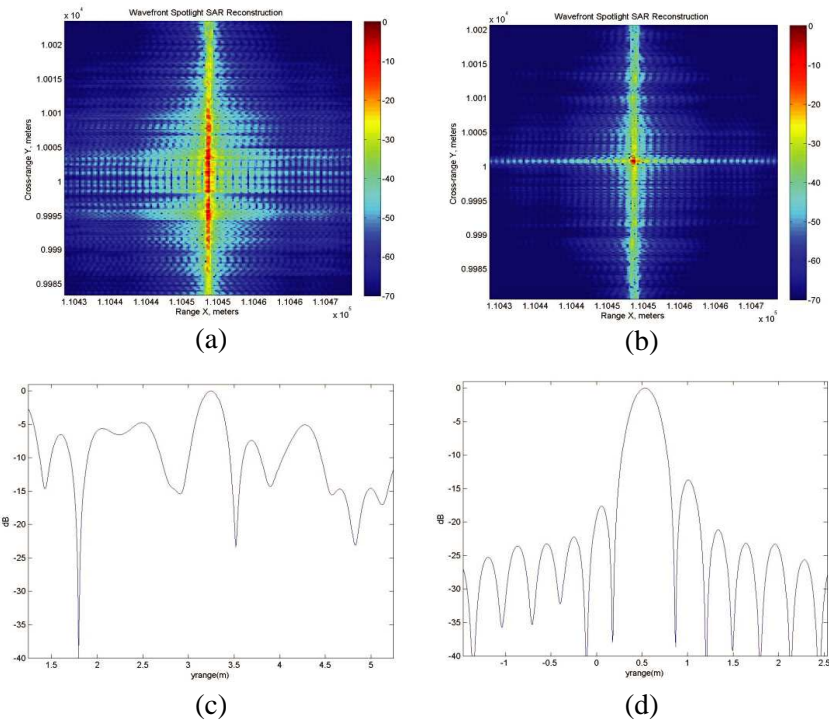**Figure 7.** AF result using 1D interpolation. (a) Before AF (SC at center). (b) After AF (SC at center).

Figure 8. Comparison before AF and after AF. (a) Before AF. (b) After AF. (c) Before AF (cross-range). (d) After AF (cross-range).

Table 3. Performance measures of cross-range profile.

Performance measure	Before AF	After AF
PSLR (dB)	−4.82	−13.72
ISLR (dB)	8.52	−10.64

scene center = [110 10 0] km and one SC at the scene center. The PSF derived using 1D interpolation was tilted and the SC was not focused due to the spreading in several range bins (Figure 7).

The PSF derived using the proposed method was cross-shaped and the quality was improved considerably after AF due to the cross-range PS spreading in a very narrow down-range (Figure 8). In the analysis of the cross-range profiles of Figure 8(b), the cross-range profile was considerably improved after AF due to the effective PSF spreading (Figures 8(c) $\sim$ (d)). Due to the usage of the entropy cost function and its minimization regardless of the shape of PSF, the cross-range profile became rather asymmetric and the PSLR became smaller than −13.3 dB which is the lower bound of the rectangular window in Fourier transform. The quality measures of the cross-range profile, peak sidelobe ratio (PSLR) and the integrated sidelobe ratio (ISLR) (see [4] for the definition), were considerably improved after AF (Table 3); improvement of PSLR was 8.90 dB and that of ISLR was 19.16 dB. Therefore, it can be concluded that the proposed method is adequate for the squint mode SAR imaging under motion errors due to turbulence.

4. CONCLUSION

In this paper, based on the aircraft trajectory under turbulence modeled using the measured spectrum data of turbulence, we proposed a squint mode MOCOM method using an efficient 2D interpolation technique for the RMA spotlight mode SAR image. In the simulation using the real trajectory, the proposed method yielded the well-formed cross-shaped PSF on the SAR image while the conventional 2D interpolation generated the ghost image due to the spatially varying interpolation error. In addition, the computation time of the proposed method was much faster than that of the conventional 2D method. At a high squint angle, Δy considerably improved. In the simulation using the measured trajectory, the PSF derived using the proposed method was successfully focused while the existing 1D interpolation yielded poor results due to squint PSF spreading.

ACKNOWLEDGMENT

REFERENCES

1. Xu, H.-Y., H. Zhang, K. Lu, and X.-F. Zeng, "A holly-leaf-shaped monopole antenna with low RCS for UWB application," *Progress In Electromagnetics Research*, Vol. 117, 35–50, 2011.

2. De Cos, M. E., Y. Alvarez Lopez, and F. Las-Heras, "A novel approach for RCS reduction using a combination of artificial magnetic conductors," *Progress In Electromagnetics Research*, Vol. 107, 147–159, 2010.

3. Gao, P. C., Y. B. Tao, and H. Lin, "Fast RCS prediction using multiresolution shooting and bouncing ray method on the GPU," *Progress In Electromagnetics Research*, Vol. 107, 187–202, 2010.

4. Soumekh, M., *Synthetic Aperturer Radar Signal Processing with MATLAB Algorithms*, John Wiley & Sons, Inc., 1999.

5. Chua, Y. M. and V. C. Koo, "FPGA-based chirp generator for high resolution UAV SAR," *Progress In Electromagnetics Research*, Vol. 99, 71–88, 2009.

6. Sun, J., S. Mao, G. Wang, and W. Hong, "Extended exact transfer function algorithm for bistatic SAR of translational invariant case," *Progress In Electromagnetics Research*, Vol. 99, 89–108, 2009.

7. Li, C. and D.-Y. Zhu, "A residue-pairing algorithm for INSAR phase unwrapping," *Progress In Electromagnetics Research*, Vol. 95, 341–354, 2009.

8. Zhang, D. Y., L. Wu, and G. Wei, "A new classifier for polarimetric SAR images," *Progress In Electromagnetics Research*, Vol. 94, 83–104, 2009.

9. Wu, I. B., M. C. Yeung, Y. Hara, and J. A. Kong, "INSAR height inversion by using 3-D phase projection with multiple baselines," *Progress In Electromagnetics Research*, Vol. 93, 173–193, 2009.

10. Wei, J. S., X.-L. Zhang, J. Shi, and G. Xiang, "Sparse reconstruction for SAR imaging based on compressed sensing," *Progress In Electromagnetics Research*, Vol. 109, 63–81, 2010.

11. Park, J. I. and K.-T. Kim, "A comparative study on ISAR imaging algorithms for radar target identification," *Progress In Electromagnetics Research*, Vol. 108, 155–175, 2010.

12. Chang, L., C.-Y. Chiang, and K.-S. Chen, "SAR image simulation with application to target recognition," *Progress In Electromagnetics Research*, Vol. 119, 35–57, 2011.

13. Wu, J., J. Yang, Y. Huang, Z. Liu, and H. Yang, "A new look at the point target reference spectrum for bistatic SAR," *Progress In Electromagnetics Research*, Vol. 119, 363–379, 2011.

14. Guo, D., H. Xu, and J. Li, "Extended wavenumber domain algorithm for highly squinted sliding spotlight SAR data processing," *Progress In Electromagnetics Research*, Vol. 114, 17–32, 2011.

15. Liu, C., X. Gao, W. Jiang, and X. Li, "Interferometric INSAR three-dimensional imaging using one antenna," *Progress In Electromagnetics Research M*, Vol. 21, 33–45, 2011.

16. Ren, X.-Z., Y. F. Li, and R. Yang, "Four-dimensional SAR imaging scheme based on compressive sensing," *Progress In Electromagnetics Research B*, Vol. 39, 225–239, 2012.

17. Ren, X.-Z., Y. Qin, and L. H. Qiao, "Interferometric properties and processing for spaceborne spotlight SAR," *Progress In Electromagnetics Research*, Vol. 36, 267–281, 2012.

18. Lim, T. S., C.-S. Lim, V. C. Koo, H.-T. Ewe, and H.-T. Chuah, "Autofocus algorithms performance evaluations using an integrated SAR product simulator and processor," *Progress In Electromagnetics Research B*, Vol. 3, 315–329, 2008.

19. Chan, Y. K., V. C. Koo, C. Y. Ang, K. S. Yee, and M. Y. Chua, "Design and development of a C-band RF transceiver for UAVSAR," *Progress In Electromagnetics Research C*, Vol. 24, 1–12, 2011.

20. Park, S.-H., M.-G. Joo, and K.-T. Kim, "Construction of ISAR training database for automatic target recognition," *Journal of Electromagnetic Waves and Applications*, Vol. 25, Nos. 11–12, 1493–1503, 2011.

21. Woo, J.-C., B.-G. Lim, and Y.-S. Kim, "Modification of the recursive sidelobe minimization technique for the range-doppler algorithm of SAR imaging," *Journal of Electromagnetic Waves and Applications*, Vol. 25, No. 13, 1783–1794, 2011.

22. Dai, C. Y. and X. L. Zhang, "Omega-K algorithm for bistatic SAR with arbitrary geometry configuration," *Journal of Electromagnetic Waves and Applications*, Vol. 25, Nos. 11–12, 1564–1576, 2011.

23. Angulo, L. D., S. G. Garcia, M. F. Pantoja, C. C. Sanchez, and R. G. Martín, "Improving the SAR distribution in petri-dish cell

cultures," *Journal of Electromagnetic Waves and Applications*, Vol. 24, Nos. 5–6, 815–826, 2010.

24. Park, S.-H., D.-H. Kim, and K.-T. Kim, "SAR motion compensation for Korean MUAV," *Asia-Pacific Int. Conf. on Syn. Aper. Radar*, Sep. 2011.

25. Li, X., G. Liu, and J. Ni, "Autofocusing of ISAR images based on entropy minimization," *IEEE Trans. Aerosp. Electron. Syst.*, Vol. 35, No. 4, 1240–1251, Oct. 1999.

26. Shin, H.-S. and J.-T. Lim, "Range migration algorithm for airborne squint mode spotlight SAR imaging," *IET Radar Sonar Navig.*, Vol. 1, No. 1, 77–82, Feb. 2007.

27. Wu. J., Y. Huang, J. Xiong, and J. Yang, "Range migration algorithm in bistatic SAR based on squint mode," *2007 IEEE Rad. Conf.*, 579–584, Apr. 2007.

28. Faires, J. D. and R. Burden, *Numerical Methods*, Brooks/Cole, 2003.

29. Jakowatz, C. V., D. E. Wahl, D. A. Yocky, B. K. Bray, W. J. Bow, and J. A. Richards, "Comparison of algorithms for use in real-time spotlight-mode SAR image formation," *Proc. of SPIE*, Vol. 5427, 108–116, Sep. 2004.

30. Kolmogorov, A. N., "Sur l'interpolation et l'extrapolation des suites stationnairres," *C. R. Acad. Sci.*, Vol. 203, 2043–2045, 1939.

31. Press, W. H., S. A. Teukolsky, W. T. Vetterling, and B. P. Flannery, *Numerical Recipes: The Art of Scientific Computing*, Cambridge University Press, 2007.